Indian Journal of Chemistry
Vol. 65, February 2026, pp. 118-127
DOI: 10.56042/ijc.v65i2.22095

Comparative study of nanostructured 3d and 4d transition metal oxides (Mn_2O_3 and TiO_2) for energy, environmental, and biomedical applications: Synthesis, characterization, and future perspectives

Gajendra Singh Lodhi[a], Jyoti Sharma*[b] & Bholey Nath Prasad[c]

[a] Seth Ganga Sagar Jatiya Government Polytechnic, Khurja, 203 131, Bulandshahar, Uttar Pradesh, India

[b] Department of Chemistry, School of Basic and Applied Sciences, Shobhit Institute of Engineering and Technology (Deemed-to-be-University), Meerut 250 110, Uttar Pradesh, India

[c] Government Polytechnic, Ayodhya 224 001, Uttar Pradesh, India

E-mail: lodhigajendra8@gmail.com

Received 28 July 2025; accepted (revised) 5 January 2026

This comparative study investigates the synthesis and characterization of Mn_2O_3 and TiO_2 nanoparticles using auto-combustion and sol-gel methods, respectively. The structural, morphological, and compositional properties of both nanoparticles have been analyzed using X-ray diffraction (XRD), Fourier-transform infrared (FTIR) spectroscopy, scanning electron microscopy (SEM), and energy-dispersive X-ray (EDX) spectroscopy. The XRD analysis reveals distinct crystal structures, with Mn_2O_3 exhibiting a cubic structure (space group $la\bar{3}$, lattice parameter a = 9.410086 Å) and TiO_2 displaying a tetragonal anatase phase (space group I41/amd, lattice parameters a = b = 3.771 Å and c = 9.43 Å). The average crystallite size of Mn_2O_3 nanoparticles has been estimated to be approximately 30 ± 5 nm using the Debye-Scherrer equation, whereas the Williamson-Hall plot reveals a crystallite size of 75 ± 5 nm and lattice micro-strain of 0.00181. In contrast, TiO_2 nanoparticles exhibit irregular and spherical shapes with clumped distribution, having average grain sizes of 0.54 µm and 0.31 µm under 10,000X and 5,000X magnifications, respectively. EDX analysis has detected the presence of Ti, O, and a small amount of S impurities in TiO_2 nanoparticles. The comparative analysis highlights the differences in structural, morphological, and compositional properties between Mn_2O_3 and TiO_2 nanoparticles, which can significantly impact their potential applications in various fields, including energy storage, catalysis, and biomedicine. This study provides valuable insights into the synthesis and characterization of these nanoparticles, paving the way for further research and development.

Keywords: Mn_2O_3NPs, TiO_2NPs, EDX, XRD, SEM, FTIR, Auto-combustion synthesis, Sol-Gel approach

Transition metal oxides have emerged as a class of materials with immense potential for various applications, owing to their unique electronic, optical, and magnetic properties. Among these, manganese sesquioxide (Mn_2O_3) and titanium dioxide (TiO_2) nanoparticles have garnered significant attention due to their distinct characteristics and potential uses in energy, environmental, and biomedical fields. Mn_2O_3, a 3d transition metal oxide, exhibits a range of fascinating properties, including high surface area, tunable morphology, and excellent electronic and magnetic properties. These attributes make Mn_2O_3 nanoparticles an attractive material for various applications, including energy storage, catalysis, and biomedicine. Mn_2O_3 nanoparticles have been explored as electrode materials in supercapacitors and lithium-ion batteries, catalysts for pollutant degradation, and contrast agents in magnetic resonance imaging (MRI). On the other hand, TiO_2, a 4d transition metal oxide, is a widely studied material due to its exceptional properties, including high refractive index, excellent optical transmittance, and photocatalytic activity. TiO_2 nanoparticles have been explored for various applications, including photocatalysis, solar energy conversion, and biomedicine. Their photocatalytic activity makes them suitable for applications such as pollutant degradation and water splitting.

In recent years, nanostructured materials particularly transition metal oxides such as NiO (Ref. 1), CuO (Ref. 2), Cr_2O_3 (Ref. 3), ZnO (Ref. 4), and Co_3O_4 (Ref. 5) have attracted significant research interest due to their unique physical and chemical properties. These properties arise from their controlled morphology, high surface-to-volume ratio, and nanoscale size, distinguishing them from their bulk counterparts. Transition metal oxides have been extensively explored in fields such as water treatment, solar energy conversion (*e.g.*, in solar cells), heterogeneous catalysis,

and magnetic resonance imaging (MRI), owing to their excellent electronic and magnetic characteristics[6–10].

Among transition metals, manganese stands out for its ability to exist in multiple oxidation states, leading to the formation of diverse oxides such as MnO, Mn_2O_3, Mn_3O_4, MnO_2, and Mn_5O_8 (Ref. 11–15). Manganese sesquioxide (Mn_2O_3), in particular, has drawn growing attention due to its environmentally benign nature, low toxicity, cost-effectiveness, structural versatility, and widespread availability. These qualities make Mn_2O_3 a multifunctional material with applications across a broad range of technologies, including hydrazine electrochemical sensing[16], electrochemical supercapacitors[17], catalysis (*e.g*., for complete oxidation of volatile organic compounds)[18], oxygen storage in catalytic systems[19], molecular adsorption[20], high-density magnetic data storage, and MRI contrast agents[21]. It also serves as a catalyst for removing greenhouse gases such as CO_2 and nitrogen oxides (NO, NO_2) from exhaust streams[22].

Additionally, due to its high theoretical specific capacity, Mn_2O_3 is considered a promising anode material for lithium-ion batteries[23]. Various synthesis methods have been employed to fabricate manganese oxides, including homogeneous precipitation[24], wet-chemical approaches[25], electrospinning[26], and thermal decomposition of manganese precursors[27], hydrothermal synthesis[28], ion-exchange methods[29], and solvothermal techniques[30]. In the present research work, Auto-combustion technique have been utilized for the preparation of Mn_2O_3 NPs at room temperature because it provides rapid, cost effective, flexible approach than the other synthesis method. Then, comprehensive characterization techniques such as powder X-ray diffraction (XRD), Fourier transform infrared (FTIR) spectroscopy scanning electron microscopy (SEM) were used to analyze the existence of phase, chemical compositions and morphology of synthesized materials.

Humans are consuming a wide range of resources these days, which results in a significant volume of organic pollutants that drastically harm the planet's natural ecosystem and need to be handled. TiO_2 powder, also referred to as titania, is nanocrystalline (nc) titanium dioxide and has garnered significant interest in light of its great potential for use in various applications, including photocatalysis, solar energy conversion, as well as its high index of refraction, good electrical conductivity, UV absorbance, hydrophobicity, superior durability, gas sensors, photovoltaics, lithium ion batteries and potential to support significant ecologically beneficial processes including water splitting to produce hydrogen and the remediation of contaminated air and water[31,3]. The variety of applications of TiO_2 in the different areas may be account of its advantageous electrical and optical characteristics, such as its high electrical resistivity, high dielectric constant, outstanding optical transmittance in the visible range, large band gap, high refractive index as well as its low-toxicity[36,3]. It is discovered that several factors affect the characteristics of nc-TiO_2 powder and, in turn, how well it performs in the specified applications[38-41]. One of the most useful variables in this scenario has been considered to be polymorphic phase transformation. Under ambient circumstances, TiO_2 may take on four distinct polymorphs: bronze TiO_2-B (C2/m), rutile (tetragonal; S.G. P42/mnm) phases, anatase (tetragonal; S.G. $I4_1/amd$) and ramdellite (Pbnm S.G.)[42,43]. Among them, rutile with tetragonal structure is often stable at high temperature. Industrial applications often use titanium dioxide in both the rutile and anatase phases. Rutile is a typical white pigment used for its exceptional optical hiding power, while anatase, with its strong photoactivity, is a helpful catalyst in photochemistry[44]. Furthermore, because of its tremendous photocatalytic ability, TiO_2 is also widely acknowledged to be one of the best semiconductor materials for degrading down organic molecules. It acts as a photocatalyst on the exposure of ultraviolet or near-visible light of the wavelength shorter than 390 nm ($E \geq E$ band gap) to TiO_2 semiconductor with suitable band structure. When the light illuminates from the light source and exposed on the semiconductor surface, generation of charge carriers *i.e*., holes from conduction band and electron from valence band. This may lead to the production of highly oxidizing superoxide radicals ($^{-}O_2$) and hydroxyl radicals ($^{\cdot}OH$), which have the ability to oxidize almost any organic substance[45-48]. Additionally, Various synthesis procedure have been documented for synthesizing TiO_2 nanoparticles, including sono-chemical, hydrothermal, coprecipitation, solvo-thermal, electrospining process, sol-gel, reverse micelles[49-55]. Because of its intrinsic qualities, which include simplicity, non-toxicity, and homogenous doping at the atomic level, the sol-gel approach is particularly concerning among them[56].

This study aims to investigate the synthesis, characterization, and potential applications of Mn_2O_3 and TiO_2 nanoparticles. By comparing the properties and performance of these two transition metal oxides, we

can gain a deeper understanding of their potential uses and limitations. The study will explore the synthesis methods, structural and morphological properties, and potential applications of Mn_2O_3 and TiO_2 nanoparticles in energy, environmental, and biomedical fields. The research is needed to fully explore the properties and applications of these nanoparticles and to develop scalable synthesis methods for their production.

Experimental Section

Synthesis of Mn_2O_3 Nanoparticles

Mn_2O_3 nanoparticles were synthesized by the auto-combustion technique using analytical-grade chemicals manganese nitrate tetrahydrate ($Mn(NO_3)_2{\cdot}4H_2O$) (Sigma Aldrich 99.9%) and citric acid monohydrate ($C_6H_8O_7{\cdot}H_2O$) (Merck, India 99%) as raw materials. These materials were dissolved in distilled water and stirred thoroughly to obtain a clear, homogeneous solution. This solution was heated at approximately 80°C on a magnetic stirrer with a hot plate to evaporate excess water, resulting in the formation of a viscous gel. On further heating, it goes through a fast, self-sustained combustion reaction, yielding fine Mn_2O_3 powder. The as-synthesized product was calcined at 500°C for 6 hours to improve crystallinity and remove any remaining organic residues.

Characterization of Mn_2O_3 Nanoparticles

The phase composition of the synthesized Mn_2O_3 nanoparticles was analyzed using X-ray diffraction (XRD) on a Rigaku Ultima IV diffractometer with a Cu-Kα radiation source (λ = 1.54 Å). XRD data were collected over a 2θ range of 10°–80° at a scan rate of 1°/min. Structural analysis, based on the cubic symmetry and space group $la\bar{3}$, was performed using Rietveld refinement. The refinement utilized a Pseudo-Voigt profile function and axial divergence symmetric background, processed through the FullProf Suite with WinPLOTR and/or EdPCR interfaces. Fourier-transform infrared (FTIR) spectroscopy was carried out using a Shimadzu IRAffinity-1S instrument in the range of 400–4000 cm^{-1} to determine the chemical composition, confirm the presence of metal–oxygen (M–O) and metal–oxygen–metal (M–O–M) bonds, and identify functional groups associated with Mn_2O_3. Surface morphology was studied using scanning electron microscopy (SEM) on a JEOL JSM-6500F instrument, operated at an accelerating voltage of 10.00 kV, with imaging performed at a 100 nm scale.

Synthesis of TiO_2 Nanoparticles

Titanium oxide (TiO_2) Nps were fabricated *via* Sol-Gel approach using titanium isopropoxide (TIP) (Ti (OCH))$(CH_3)_2)_4$) as precursors. For this, a solution of TiP was added in to mixture of ammonium sulphate in the molar ratio of 1:6 and then water is added drop-wise in the resulting mixture with continuous stirring on hot plate at 70°C. Formation of oxide network occurs in this condition and further, required concentration of citric acid was added in the resulting mixture with continuous stirring for proper mixing. An extremely viscous white sol-gel was produced after an hour of continuous stirring at 70°C with a mixture of strong sulfuric acid and deionized water added to the titanium isopropoxide solution. After heating the gel to 200°C for 2 hours, a puffy, polymeric citrate precursor was formed. After finely powdering the precursor, TiO_2 nanoparticles were calcined in an electrical furnace for 5 hours at 600°C. Titanium alkoxide (TIP or Ti(OR)n) is hydrolyzed and condenses resulting in titanium hydroxide, which is then used to synthesis TiO_2 nanoparticles typical achieved by sol-gel process.

$(Ti(OCH))(CH_3)_2)_4) + 4H_2O \rightarrow Ti(OH)_4 + 4(CH_3)_2CHOH$ (hydrolysis)

The precursor, which is converted into the titanium oxide network, is hydrolyzed with the assistance of acid or base in addition to alcohol.

$Ti(OH)_4 \rightarrow TiO_2 \downarrow + 2H_2O$ (condensation)

Subsequently, using a hydraulic press, the two-thirds of PVA was combined with the calcined TiO_2 powder and formed into cylindrical pellets. The pellets were then heated for two hours at 350°C to remove the PVA binder, and the pellets were utilized for various physiochemical characterizations.

Characterization of TiO2 Nanoparticles

Using the Rigaku D/max-2400 model, Cu-Ka radiation (40 kV, 60 mA)-based X-ray diffraction (XRD) was used to study the phase identification of the materials from 2θ range of 20°–80° along with step size of 0.02° and scan rate of 1 deg min^{-1}. Using a NETZSCH apparatus of the type STA 449 F3, which was run at 10◦C min^{-1} from RT to 900 ◦C, granulated TiO2 particles were employed for thermal gravimetric analysis (TGA) and differential scanning calorimetry (DSC). A secondary electron detector on a JEOL JSM-6390A scanning electron microscope (SEM) operating at a distance of 14.9 mm and electron energy

of 20.0 kV was used to study the microstructures. This experiment, called SEM-EDS (Energy Dispersive Spectroscopy), was conducted with a JEOL JSM-6390A SEM from Japan, equipped with an EDAX, Inc. EDS detector and EDX; Kevex, Sigma KS3 software. The spectra were acquired at an accelerating voltage of 15.0 kV and a working distance of 14.5 mm. Before investigation, a 150 × 150 µm zone coated with particles was covered with Titania particles, and spectrum data was taken on that zone.

Results and Discussion

Mn_2O_3 Nanoparticles

The morphology and phase purity of the as-synthesized Mn_2O_3 nanoparticles were examined using X-ray diffraction (XRD) from 2θ range of 10-80° as described in Fig. 1. As seen from figure that there is no existence of any other impurities peaks besides the peaks of host-materials which is verified *via* JCPDS card No. 24-0508 (Ref. 57). The distinctive peaks appears at the different 2θ values are indexed with the respective (hkl) crystal planes as shown in figure are consistent with JCPDS data, confirming the presence of pure cubic structure of Mn_2O_3 nanoparticles. Additionally, the prominent peak observed around 2θ ≈ 33.00° indicates a high degree of crystallinity in the synthesized nanoparticles. The lattice parameter (a) of Mn_2O_3 nanoparticles was calculated to be 9.4101 Å, using the interplanar spacing (d) and Bragg's law, based on the following relation:

$$a = \frac{\lambda\sqrt{(h^2+k^2+l^2)}}{2\sin\theta} \quad ...(1)$$

where λ is the wavelength of the Cu-Kα radiation (1.54 Å), *(hkl)* are the Miller indices, and θ is the Bragg angle. The average crystallite size (D) was estimated using the Scherrer formula $D = {k\lambda}/{\beta Cos\theta}$, where, k, λ, β and θ represent Scherrer constant with the value of 0.94, wavelength of CuKα radiation (1.54 Å), full width at half maximum (FWHM) of the diffraction peak (corrected for instrumental broadening) and Bragg's angle. The mean crystallite size of the cubic Mn_2O_3 nanoparticles, based on the analysis of prominent *(hkl)* planes, was found to be approximately 30 ± 5 nm.

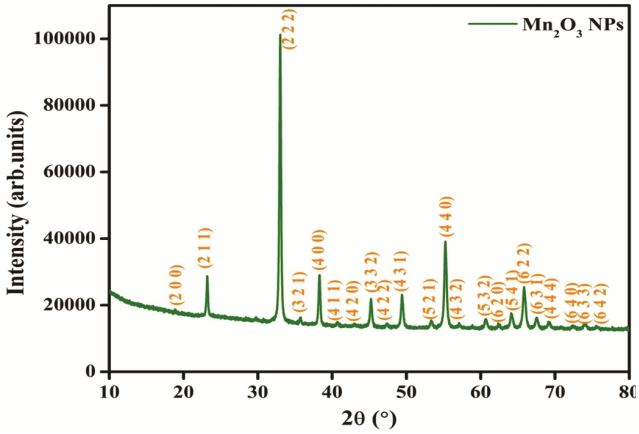

Fig. 1 — X-ray diffraction (XRD) pattern of fabricated Mn_2O_3 nanoparticles sintered at 500°C for 6h.

Additionally, the broadening in the XRD peaks was occurred a in the materials due to contributions of lattice strain and the crystallite size which may be commonly evaluated by using Uniform Deformation Model (UDM). Based on the assumption of this model, it was observed that the defects in the crystal lattice arose due to a uniform distribution of strain across all crystallographic directions[58]. The broadening in XRD peaks due to an occurrence of micro-strain can be evaluated mathematically using following equation,

$$\beta_{strain} = 4\,\varepsilon\tan\theta \quad ...(2)$$

Where, the symbol β_{strain} indicates full width at half maxima (FWHM) due to lattice strain and ε due to micro-strain, respectively. On the other hand, the broadening caused by crystallite size (D) in the XRD peaks calculated by using the relations given by Debye- Scherrer formulae,

$$\beta_D = \frac{k\lambda}{\mathrm{D}\cos\theta} \quad ...(3)$$

The total broadening (β_{hkl}) occurred in the XRD peaks due to crystallite size (D) and due to lattice micro-strain can be obtained by combining the above equation (2 and 3), is that

$$\beta_{hkl} = \beta_{strain} + \beta_D = 4\,\varepsilon\tan\theta + \frac{k\lambda}{\mathrm{D}\cos\theta} \quad ...(4)$$

On rearranging above Eq^n (4), results the straight line equation (5) having intercept, $\frac{k\lambda}{D}$ and slope (ε) obtained by plotting the graph between $4\sin\theta$ on X-axis and $\beta_{hkl} \times \cos\theta$ on Y-axis.

$$\beta_{hkl} \times \cos\theta = \left(\frac{k\lambda}{D}\right) + 4\varepsilon\sin\theta \quad ...(5)$$

The above equation (5) represents Williamson-Hall (W-H) equation. The crystallite size (D) and lattice micro-strain (ε) measured by W-H plot of the synthesized materials as depicts in Fig. 2, were observed to be 75 ± 5 nm and 0.00181, respectively[59].

The exact justification of morphology and formation of phase of as synthesized materials was also confirmed through Reitveld analysis from 2θ range of 10-80° by using axial divergence symmetric background and Pseudo-Voigt profile function.

This analysis was run by Fullprof Suite software *via* the WinPLOTR and/or EdPCR interfaces using Cu Kα radiation with wavelength, λ = 1.54 Å by taking step size of 0.02°/s. A proper overlapping between red dots and black dots described by observed intensity and calculated intensity, respectively are clearly visible, as can seen from the Fig. 3 which emphasized the best fitting of XRD data that can be also proved through the lower value of χ^2. All the parameters obtained during the refinement conditions of Mn_2O_3 NPs are enclosed in the Table 1 confirmed the presence of single phase formation with no characteristic peaks of other foreign impurities[60].

The appearance of various peaks in the FTIR spectrum of the Mn_2O_3 NPs in the wavenumber range of 400-4000 cm^{-1} is displayed in Fig. 4. The three

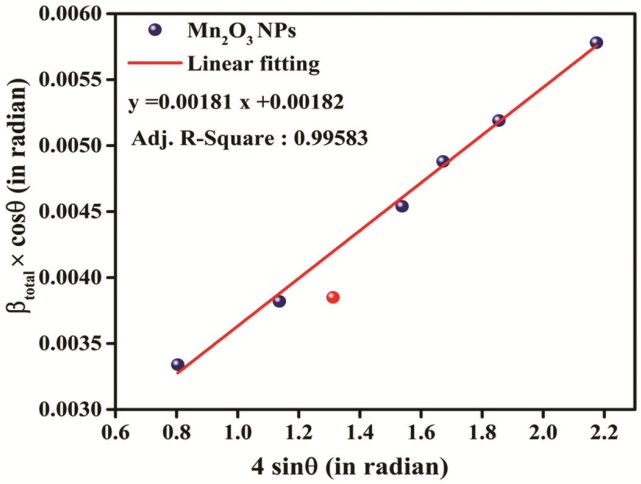

Fig. 2 — Williamson-Hall (W-H) plots of Mn2O3 nanoparticles.

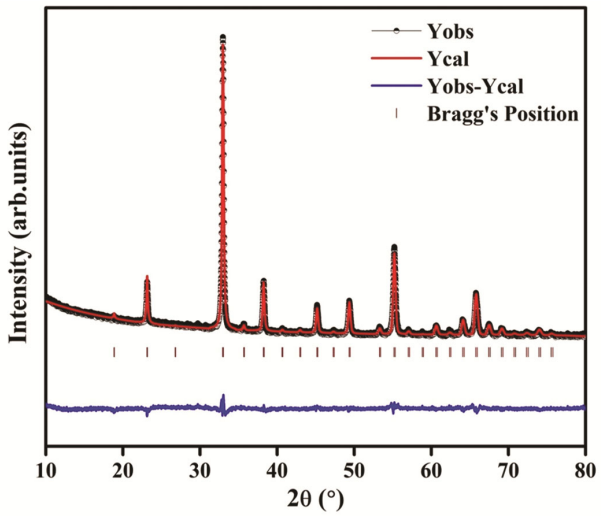

Fig. 3 — Reitveld refinement analysis of XRD data for synthesized materials in which respective red and black line indicate observed and calculated pattern, vertical line (purple color) indicates difference of observed and calculated data and blue line shows Bragg's positions.

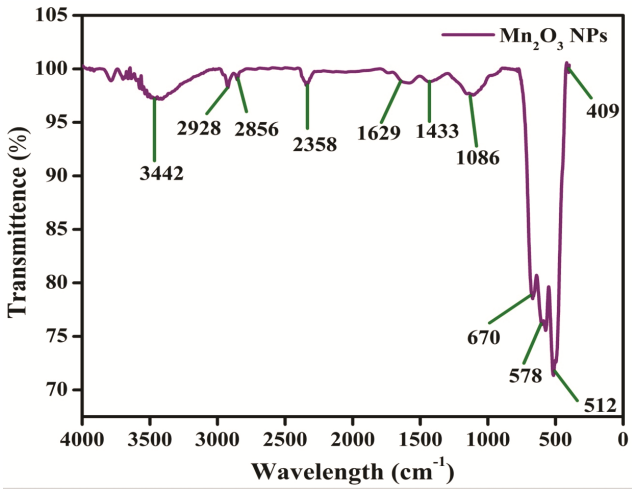

Fig. 4 — FTIR spectrum of Mn_2O_3 nanoparticles sintered at 500°C for 6h.

Table 1 — Rietveld refinement parameters of the XRD data for Mn_2O_3 nanoparticles synthesized by Auto-combustion route at sintering temperatures, at 500°C for 6 hours

χ^2	5.16	Goodness of fit, GOF= $\frac{R_{wp}}{R_{exp}}$	2.273
space group	$la\bar{3}$	Overall B-factor	0.46847
Structure	Cubic	–	–
Lattice parameters (Å)	a = 9.410086	–	–
Cell volume, Vcell ($Å^3$)	74.862308	Angel (°)	α = β = γ = 90.00
FWHM parameters	U= 0.327792	V= -0.003004	W= 0.015798
Bragg R-Factor (%)	8.745	RF-Factor (%)	6.122
Conventional Rietveld R-Factors (%)	R_p = 25.8	R_{wp}= 12.8	R_{exp}= 5.63

Number of cycle, step size and wavelength (λ) used during the refinement of XRD data are taken as 20, 0.01°/min and1.54 Å, respectively.

absorption peaks observed in the spectra of synthesized material located at respective wavenumber 409, 512, and around 670 cm^{-1} are attributed to stretching vibration of M-O bonds[61]. Another peaks appearing at around 578 cm^{-1} are assigned to be M-O-M (Mn-O-Mn) bonds due to asymmetric and bending mode of vibrations, respectively[62]. Furthermore, the presence of a weak absorption peaks clearly visible in FTIR spectrum at 1086 cm^{-1} indicates combined attaching vibrations of Mn atom with –OH groups and two peaks due to O-H stretching and bending vibrations of H_2O molecules adsorbed on the surface of Mn_2O_3 nanoparticles are in respective wavenumber regions of 1629 and 3442 cm^{-1} (broad absorption peak).

Another peaks associated with C-H stretching vibrations located at 2800-2900 cm^{-1}, suggesting the presence of hydrocarbons on the surface of Mn_2O_3 NPs (Ref. 63). Additionally, there are two distinctive peaks at 1433 and 2331 cm^{-1}, respectively also detected in the synthesized materials which may be due to O=C=O stretching and bands of CO_3^{2-} (Ref. 63). The above mentioned observation seen in the FTIR spectra confirmed the absence of any other characteristic peaks of impurities, justifying the formation of Mn_2O_3 materials.

Scanning electron microscopy (SEM) study was done for further investigation of morphology of manganese oxide (Mn_2O_3) nanoparticles and this measurement were carried out on 100 nm scale and magnification of 100,000X along with an accelerating voltage, 10 kV as mentioned in Fig. 5 (a).

Non-uniform distribution of grains with cubical nature has been clearly notice in the SEM image and also agglomeration of the Mn_2O_3 nanoparticles appearing due to combination of small particles results in the formation of bigger size particles. The existence of some porosity has been detected in the morphology of as synthesized materials. The average grain size of sample is calculated by using Image J software and observed in the range of 35 ±5 nm which is in accordance with measured crystallite size obtained through XRD results. The grain size measured through Image J software in the SEM morphology is justified by Histogram plots as depicts in the Fig. 5 (b).

TiO_2 Nanoparticles

XRD analysis is an environmentally friendly way for evaluating crystalline materials and it was utilized to determine the phase purity of TiO_2 crystal as well as characteristics like crystal structure, crystal defects, average grain size, and craystallinity of the materials. For this, XRD spectrum for TiO_2 sample was recorded from the diffraction angle (2θ) range of 20-80° with the scan rate of 1 ◦/min. It is revealed from the XRD spectra that the peaks appeared at 25.23° corresponding to the (1 0 1) plane are predominant, demonstrates the observation of higher crystallization along that plane and other weak reflections observed at diffraction angle 37.61, 48.01°, 53.67°, 54.92°, 62.66°, 68.62°, 70.32°, 74.79° were consistent with the respective planes (1 0 3), (2 0 0), (1 0 5), (2 1 1), (2 1 3), (1 1 6), (2 2 0) and (1 0 7) (Fig. 6).

All these reflection peaks are well matched with the ICDD Number #01-071-1167. Further, the

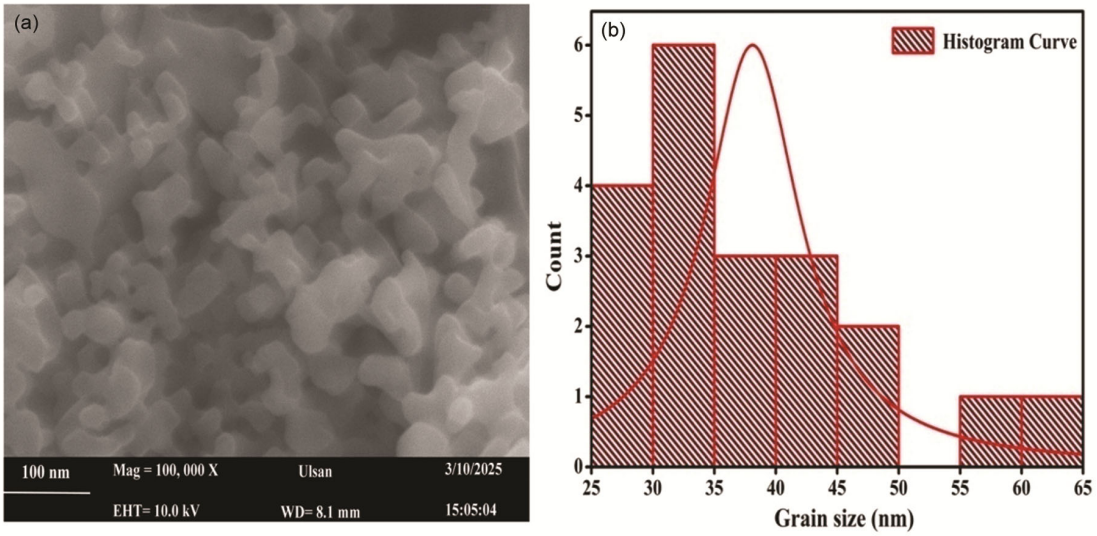

Fig. 5 — (a) SEM morphology (b) Histogram plots of synthesized Mn_2O_3 nanoparticles.

XRD pattern shows no diffraction peaks corresponding to impurity representing high purity and the presence of predominant peaks with respect to the plane (101) confirmed the tetragonal crystal structure of anatase TiO_2. Subsequently, the full width-half maxima were used to estimate the crystallite sizes (D) relative to all diffraction peaks by using Debye-Scherrer equation[65] and the results were summarized in the Table 2.

Thermogravimetric analysis (TGA) as well as derivative of thermogravimetric analysis (DTA) was recorded from RT to 850°C on the scanning rate (10°C/min) for investigation of thermal stability and crystalline state of TiO_2 powders, as depicts in Fig. 7. Four types of weight loss were noted in the TGA curve in which initial step of a small weight loss (0.84%) appeared in the temperature range of 45-200°C corresponding to the loss of water and moisture[66]. After which, the next subsequent decrease in weight (1.53%) between 200° and 350°C may be related to the decomposition of organic materials and nitrate ions in the samples[67].

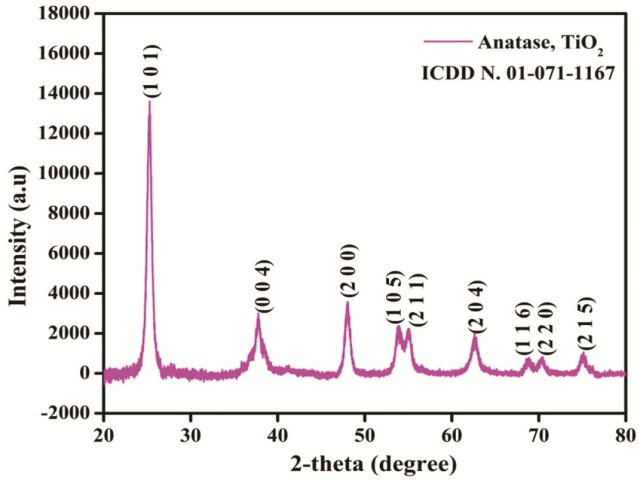

Fig. 6 — Powder X-ray diffraction pattern of TiO_2 particles at the calcination temperature of 1150°C for 3 hrs.

Furthermore, another weight loss (1.68%) observed between 350 - 400°C may be due to the occurrence of less impurity in the materials and the weight loss (1.69%) between 450°C and 640°C emphasized a phase transition from amorphous TiO_2 to crystalline anatase[68]. No appreciable change in the mass was noticed in the sample after the temperature of 640°C emphasized removable of organics and any other impurities and also indicating thermal stability of TiO_2. Furthermore, distinct abrupt exothermic reaction peaks emerged at various temperatures, as seen by the DTA curves, showing a phase transition of the powder from amorphous to anatase.

To identify the morphological characteristics of TiO_2 materials, scanning electron microscopy were scanned over two different magnifications (10,000X and 5,000X) as indicated in Fig. 8 (a and b). It is clearly revealed from SEM image that the presence of irregular shape of TiO_2 nanoparticles at 10,000X magnification and Clumped distribution of particles with spherical shaped were seen at lower magnification (5,000X) (Ref. 69).

The average value of grain size obtained through Image J software under higher and lower magnification

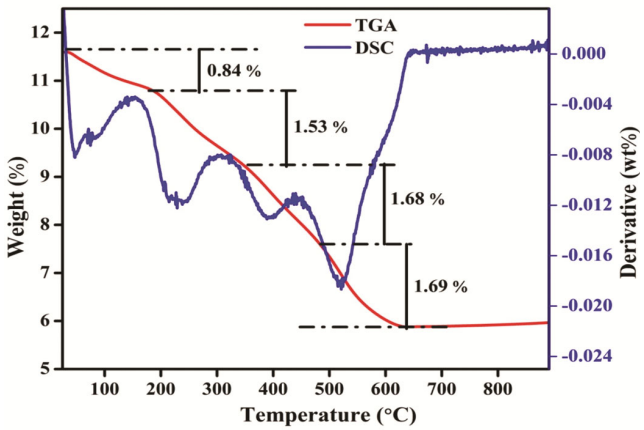

Fig. 7 — Shows TG-DTA curve of TiO_2 nanoparticles measured from RT- 900°C.

Table 2 — Represents 2-θ, full-width at half maxima (FWHM), D-values, d-spacing, different planes with respect to anatase phase

2-θ (deg)	d (angle)	FWHM(deg)	Crystallite size (D) (nm)	Plane corresponding Anatase phase
25.23	3.5257	0.646	13.16	(1 0 1)
37.60	2.3899	1.192	7.36	(1 0 3)
47.95	1.8953	0.713	12.7	(2 0 0)
53.67	1.7063	1.59	5.84	(1 0 5)
54.92	1.6703	0.44	21.1	(2 1 1)
62.66	1.4814	1.013	9.59	(2 1 3)
68.62	1.3666	0.90	11.1	(1 1 6)
70.32	1.3377	0.87	11.7	(2 2 0)
74.80	1.2682	1.19	8.8	(1 0 7)

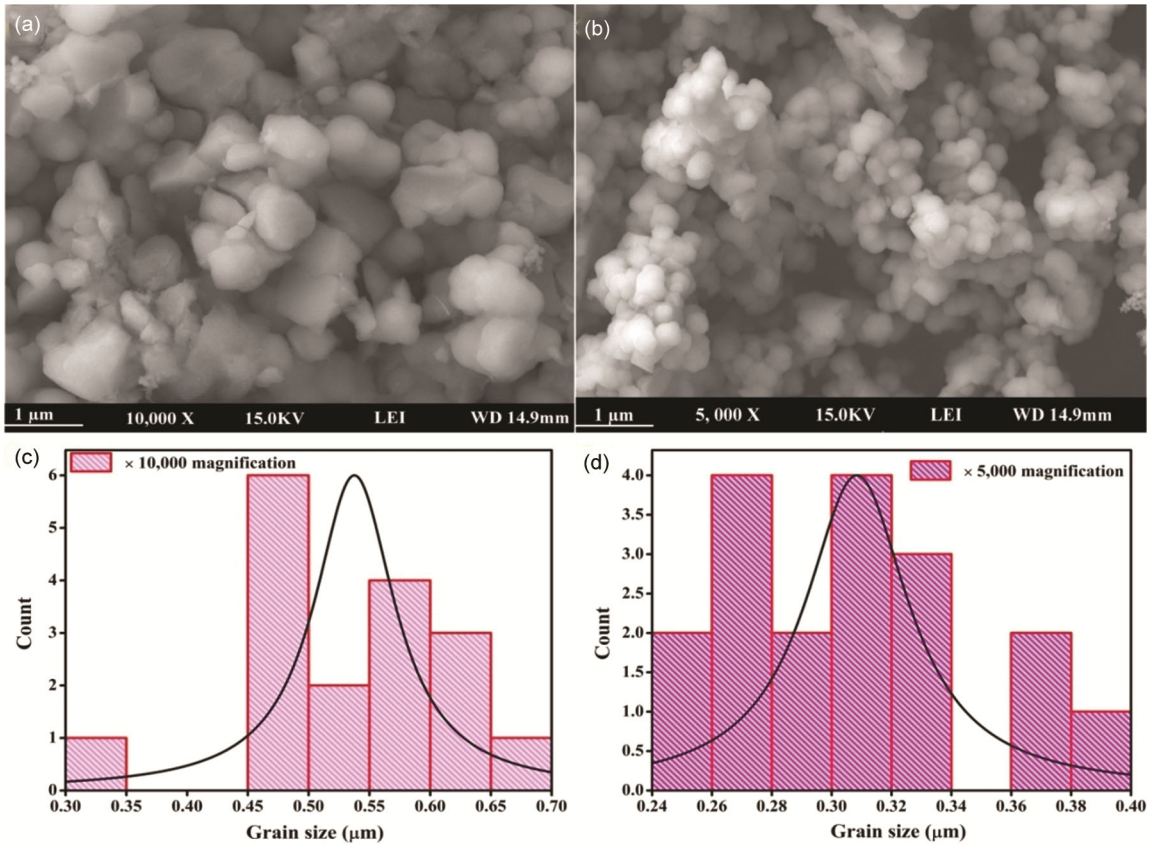

Fig. 8 — (a and b) depict SEM micrograph of TiO_2 NPs at 10,000X and 5,000X resolution, (c and d) represent histogram distribution curve corresponding to high and low magnification.

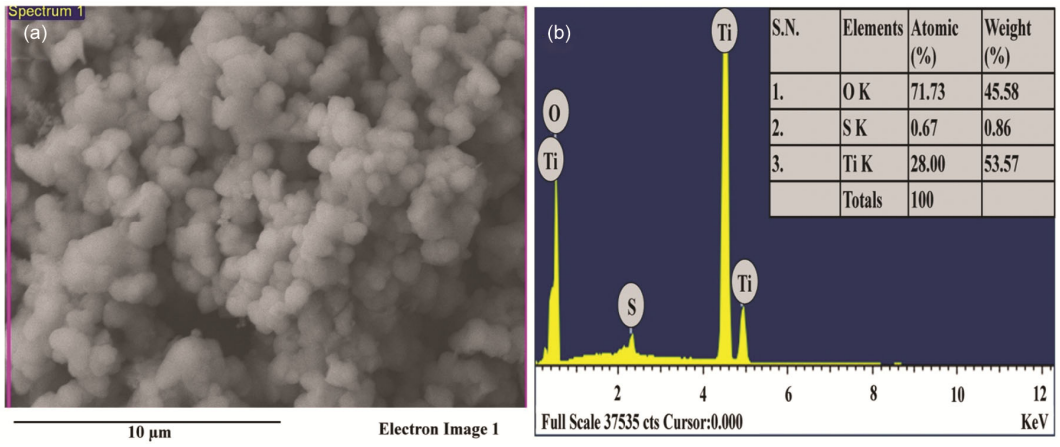

Fig. 9 — (a) Cross sectional SEM micrograph (b) EDX pattern corresponding to SEM image of TiO_2 NPs.

were found to be 0.54 µm, 0.31µm, respectively which have the similar results observed through histogram plot as depicts in the Fig. 8 (c and d).

Fig. 9 (a and b) demonstrate cross sectional SEM image measured on the 10 µm scale and Energy dispersive X-ray (EDX) spectra of TiO_2 nanoparticles. From Fig. 9a, it is revealed that TiO_2 particles exhibit some of spherical shaped as well as irregular shaped with clumped distribution of particles and some of the porosity is also seen in the morphology of TiO_2.

The average grain size estimated through Image J software and observed to be 0.8 µm. The chemical composition of the material was analyzed by using EDX analysis as indicated by Fig. 9(b). This spectrum

confirmed the presence of Ti, O and S elements, which shows the occurrence of smaller impurities of S in the TiO_2 nanoparticles[70]. The atomic percentage as well as weight percentage for corresponding elements is disclosed in the inset of figure.

Conclusion

This study successfully synthesized Mn_2O_3 and TiO_2 nanoparticles using auto-combustion and sol-gel methods, respectively. The structural, morphological, and compositional properties of the nanoparticles were characterized using various techniques, including XRD, FTIR, SEM, and TGA.

The auto-combustion method yielded single-phase Mn_2O_3 nanoparticles with a cubic crystal structure, as confirmed by XRD and Rietveld refinement analysis. The calculated lattice parameter (a) was 5.7235 Å, and the mean average crystallite size (D) was 30 ± 5 nm. The W-H plot revealed a crystallite size of 75 ± 5 nm and lattice micro-strain of 0.00181. FTIR spectroscopy confirmed the presence of Mn-O and Mn-O-Mn bonds, and SEM images showed cubical particles with an average grain size of 35 ± 5 nm.

The sol-gel method successfully fabricated anatase TiO_2 nanoparticles with a tetragonal crystal structure, as confirmed by XRD data. The lattice parameters a = b = 3.771 Å and c = 9.43 Å corresponded to the tetragonal crystal structure of anatase TiO_2. TGA analysis revealed thermal stability of TiO_2 after 640°C. SEM morphology showed irregular and spherical particles with clumped distribution, and the average grain size was calculated to be 0.54 μm and 0.31 μm under 10,000X and 5,000X magnifications, respectively.

In conclusion, this study provides valuable insights into the synthesis, characterization, and potential applications of Mn_2O_3 and TiO_2 nanoparticles. The findings demonstrate the potential of these nanoparticles in various fields, and further research can unlock their full potential.

Future Scope

This study highlights the potential of Mn_2O_3 and TiO_2 nanoparticles in various applications, including energy storage, catalysis, and biomedicine. Potential areas for future research include:

Energy Storage Applications: Further investigation into the electrochemical properties of Mn_2O_3 and TiO_2 nanoparticles could lead to advancements in supercapacitor and lithium-ion battery technologies.

Catalytic Applications: Research into the catalytic activity of Mn_2O_3 and TiO_2 nanoparticles could explore their potential for pollutant degradation, fuel cells, and other industrial applications.

Biomedical Applications: Studying the bio-compatibility and potential uses of Mn_2O_3 and TiO_2 nanoparticles in biomedical fields, such as MRI contrast agents and drug delivery systems, could lead to innovative solutions for medical applications.

These future research directions could provide valuable insights into the properties and applications of Mn_2O_3 and TiO_2 nanoparticles, driving advancements in various fields.

References

1 Zhu Y, Guo H, Wu Y, Cao C, Tao S & Wu Z, *J Mat Chem A*, 2 (2014) 7904.
2 Raul P K, Senapati S, Sahoo A K, Umlong L M, Devi R R, Thakur A J & Veer V, *R Soc Chem Adv*, 4 (2014) 40580.
3 Pei Z & Zhang X, *Mat Lett*, 93 (2013) 377.
4 Pushpanathan V & Kumar S D, *J Nanostruc Chem*, 4 (2014) 95.
5 Makhlouf S A, Bakr Z H, Aly K I & Moustafa M S, *Superlat Micro*, 64 (2013) 107.
6 Sharrouf M, Awad R, Roumie M & Marhaba S, *Mat Sci Appl*, 6 (2015) 850.
7 Rutz A, *Mat Sci Appl*, 7 (2009) 98–99.
8 Kim D K, Zhang Y, Kehr J, Klason T, Bjelke B & Muhammed M, *J Magn Magn Mater*, 225 (2001) 256.
9 Rudder J, Wiele T V, Dhooge W, Comhaire F & Verstraete W, *Artic Water Res*, 38 (2004) 184.
10 Julien C M, Massot M & Poinsignon C, *Periodic Struct Mol Biomol Spec*, 60 (2004) 689.
11 Najjar R, Awad R & Abdel-Gaber A M, *J Supercond Novel Mag*, 32 (2019) 885.
12 Yue J, Gu X, Chen L, Wang N, Jiang X, Xu H, Yang J & Qian Y, *J Mat Chem A*, 2 (2014) 17421.
13 Han Y F, Chen F, Zhong Z, Ramesh K, Chen L & Widjaja E, *J Phys Chem B*, 110 (2006) 24450.
14 Chen Z, Jiao Z, Pan D, Li Z, Wu M, Shek C H, Wu C L & Lai J K, *Chem Rev*, 112 (2012) 3833.
15 Yue J, Gu X, Chen L, Wang N, Jiang X, Xu H, Yang J & Qian Y, *J Mat Chem A*, 2 (2014) 17421.
16 Eremenko A V, Dontsova E A, Nazarov A P, Evtushenko E G, Amitonov S V, Savilov S V, Martynova L F, Lunin V V & Kurochkin I N, *Electroanalysis*, 24 (2012) 573.
17 Komaba S, Tsuchikawa T, Ogata A, Yabuuchi N, Nakagawa D & Tomita M, *Electrochim Acta*, 59 (2012) 455.
18 Qiu G, Huang H, Dharmarathna S, Benbow E, Stafford L & Suib S L, *Chem Mat*, 23 (2011) 3892.
19 Chang Y F & McCarty J G, *Cat Today*, 30 (1996) 163.
20 Liao M Y, Lin J M, Wang J H, Yang C T, Chou T L, Chong N S & Tang H Y, *Electrochem Comm*, 5 (2003) 312.
21 Talebi R, *J Mat Sci Mat Elect*, 28 (2017) 8316.
22 Baldi M, Escribano V.S, Amores J M G, Milella F & Busca G, *App Catal B Env,* 17 (1998) 175.
23 Song C, Li R, Liu F, Feng X, Tan W & Qiu G, *Electrochim Acta*, 55 (2010) 9157.
24 Chen Z W, Lai J K L & Shek C H, *J Non-Cryst Solid*, 352 (2006) 3285.
25 Rahaman H, Laha R.M, Maiti D.K & Ghosh S K, *RSC Adv*, 5(2015) 33923.

26 Shao C, Hongyu, G, Yichun, L, Xiliang L & Xinghua Y, *J Solid State Chem*, 177 (2004) 2628.
27 Pudukudy M, Yaakob, Z & Rajendran R, *Mat Lett*, 136 (2014) 85.
28 Chen Y, Zhang Y, Yao Q.Z, Zhou G.T, Fu S & Fan H, *J Solid State Chem*, 180 (2007) 1218.
29 Zanyong Z, Chen H, Lin Z & Dang Z, *Env Sci: Nano*, 3 (2016) 1254.
30 Niu X, Wei H, Tang K Liu W, Zhao G & Yang Y, RSC Adv, 5 (2015) 66271.
31 Yi Z, Chen Y, Chen S, Tan X L, Niu G, Luo J S & Tang Y & Yi Y, *J Cent South Uni Technol*, 18 (2011) 1877.
32 Paola A D, Cufalo G, Addamo M, Bellardita M, Campostrini R, Ischia M, Ceccato R & Palmisano L, *Colloids Surf A*, 317 (2008) 366.
33 Cheng-Yu K & Shih-Yuan L, *Nanotechnology*, 19 (2008) 095705.
34 Yildiz A, Lisesivdin S B, Kasap M & Mardare D, *J Mater Sci: Mater Ele*, 21 (2010) 692.
35 Kovtyukhova N, Ollivier P, Chizhik S, Dubravin A, Buzaneva E, Gorchinskiy A, Marchenko A & Smirnova N, *Thin Solid Films*, 337 (1999) 166.
36 Jeong S H, Kim B S, Lee B T, Park H R & Kim J K, *J Korean Phys Soc*, 41 (2002) 67.
37 Akl A A, Kamal H & Abdel-Hady K, *App Surf Sci*, 252 (2006) 8651.
38 Francioso L, Presicce D.S, Taurino A M, Rella R, Siciliano P & Ficarella A, *Sensors & Actuators B*, 95 (2003) 66–72.
39 Billika P, Plescha G, Brezova V ´ b, Kuchtaa L, Valkob M & Mazu M B, J Phys Chem Solids, 68 (2007) 1112.
40 Dodd A, McKinley A, Tsuzuki T & Saunders M, *J Phys Chem Solids*, , 68 (2007) 2341.
41 Zhang L, Xu L, Wang J, Cai J, Xu J, Zhou H, Zhong Y, Chen D, Zhang J & Cao C N, *J Elect Chem*, 683 (2012) 55.
42 Rezaee M & Khoie Mousavi S M, *J Alloys Comp*, 507 (2010) 484.
43 Zhu J, Yu J-X, W Y-J, C X-R & J F-Q, *Chin Phys B*, 17 (2008) 2216.
44 W Li , Ni C, Lin H, Huang C P & Shah S I, *J Appl Phys*, 96 (2004) 6663.
45 Wolfrum E J, Huang J, Blake D M, Maness P C, Huang Z, Fiest J & Jacoby WA, *Env Sci Tech*, 36 (2002) 3412.
46 Natarajan T S, Bajaj H C & Tayade R J, *J Coll Interface Sci*, 433 (2014) 104.
47 Chen Y, Chen D, Chen J, Lu Q, Zhang M, Liu B, Wang Q & Wang Z, J Alloys Comp, 651 (2015) 114.
48 Xiao F X, Hung S F, Miao J, Wang H Y, Yang H & Liu B, *Small*, 11 (2015) 554.
49 Saroj S, Singh L & Singh S V, *J Photochem Photobio A: Chem*, 3961 (2020) 112532.
50 Kumar A, Yadava S S, Singh L, Kumar V, Verma M K, Singh S & Mandal K D, *Spie Digi Lib*, 109790 (2019) ; https://doi.org/10.1117/12.2518203.
51 Saroj S, Singh L, Ranjan R & Singh S V, *Res Chem Int*, 45 (2019) 1883.
52 Zhang Y, H Zheng, G Liu, V Battaglia, *Electrochim Acta*, 54 (2009) 4079.
53 Saroj S, Singh L & Singh S V, *Int J Chem Kinet*, 51 (2019) 189.
54 Shahruz N & Hossain, M M, *World Appl Sci J*, 12 (2011) 1981.
55 Madhvi S S, Singh L, Lee Y & Singh S V, *J Mater Sci: Mater Elect*, 27 (2016) 2581.
56 Wang X, Liu S, Guo Y, Wang Z, Li X, Ren Y, Xia Z, Wang H, Liu C, Wang N, Jiang W, Ding W & Zhang Z, *Ceram Int*, 46 (2020) 17659.
57 Deng Y, Li Z, Shi Z, Xu H, Peng F & Chen G, *RSC Adv*, 2 (2012) 4645.
58 Mote V D, Purushotham Y & Dole B N, *J Theor App Phys*, 6 (2012) 6.
59 Pati J, Priyadarshinee S, Mahapatra R, Mishra D K, Mohapatra J & Mohanty P, *Mat Today: Proc*, 67 (2022) 1080.
60 Kumari K, Kumar S, Huh S H, Kumar A, Kim M S, Shin M J, Devi N & Koo B H, *J Elec Mat*, 51 (2022) 5842.
61 Souri M, Hoseinpour V, Shakeri A & Ghaemi N, *Nanobiotechnology*, 12 (2018) 822.
62 Salavati-Niasari M, Esmaeili-Zare M & Gholami-Daghian M, *Adv Powder Tech*, 25 (2014) 879.
63 Khalaji A & Ghorbani M, *Acta Phys Polonica A*, 133 (2018) 7.
64 Mousavi S H, Yaghoobi M & Asjadi F, *Sci Rep*, 14 (2024) 18505.
65 Kumar A, Yadava S S, Singh L, Verma M K, Singh N B & Mandal K D, *J Magnet Mag Mat*, 527 (2021) 167807.
66 Khatua C, Chinya I, Saha D, Das S, Sen R & Dhar A, *Int J Smart Sens Intel Sys*, 8 (2015) 1424.
67 Sivakumar S, Pillai P K, Mukundan P & Warrier K G K, *Mat Lett*, 57 (2002) 330.
68 Kim M G, Kang J M, Lee J E, Kim K S, Kim K H, Cho M & Lee S G, *ACS Omega*, 6 (2021) 10668.
69 Hunge Y M, Yadav A A & Mathe V L, *J Mat Sci Mat Elect*, 29 (2018) 6183.
70 Ramazani M, Farahmandjou M & Firoozabadi T P, *Int J Nanosci Nanotech*, 11 (2015) 115.